

# New Synthesis of MCM-48 Nanospheres and Facile Replication to Mesoporous Platinum Nanospheres as Highly Active Electrocatalysts for the Oxygen Reduction Reaction

Po-Kai Chen,<sup>†</sup> Nien-Chu Lai,<sup>†</sup> Chia-Hua Ho,<sup>†</sup> You-Wei Hu,<sup>†</sup> Jyh-Fu Lee,<sup>‡</sup> and Chia-Min Yang<sup>\*,†,§</sup>

<sup>†</sup>Department of Chemistry, National Tsing Hua University, Hsinchu 30013, Taiwan

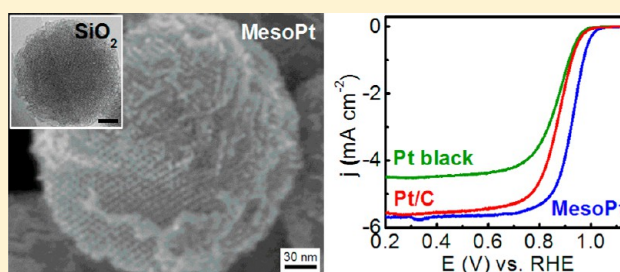
<sup>‡</sup>National Synchrotron Radiation Research Center, Hsinchu 30076, Taiwan

<sup>§</sup>Frontier Research Center on Fundamental and Applied Sciences of Matters, National Tsing Hua University, Hsinchu 30013, Taiwan

## S Supporting Information

**ABSTRACT:** Self-supported mesoporous Pt nanospheres are prepared by the templated method for the electrocatalytic oxygen reduction reaction (ORR). Single-crystal-like MCM-48 nanospheres, synthesized via a new and simple route in a dilute and alkaline solution of benzylcetyldimethylammonium chloride, are applied as the hard template. A facile process of molten salt impregnation followed by hydrogen reduction is developed to replicate both the mesostructure and morphology of the hard template and to form mesoporous Pt nanospheres. The high-surface-area mesoporous Pt nanospheres are thermally stable in air up to 300 °C without showing significant metal sintering. Electrocatalytic studies reveal that mesoporous Pt nanospheres have a large fraction of {110} facets and exhibit high activity for the ORR. The excellent electrocatalytic performance may be mainly attributed to the facet-dependent ORR activities as well as the presence of 3D interconnected mesopores to facilitate mass transport.

**KEYWORDS:** mesoporous MCM-48 nanospheres, mesoporous Pt nanospheres, nanocasting, molten salt impregnation, oxygen reduction reaction



## 1. INTRODUCTION

Low-temperature fuel cells, including proton-exchange membrane fuel cells (PEMFCs, operating at 50–100 °C) and phosphoric acid fuel cells (PAFCs, operating at 150–210 °C), are promising sustainable power sources for stationary, transport, and portable applications.<sup>1–5</sup> For these fuel cells, platinum remains among the most effective electrocatalysts for the reactions at both the cathode and anode,<sup>1–9</sup> and most Pt catalysts consist of small (2–5 nm) Pt nanoparticles that are highly dispersed on carbon supports to result in high electrochemical surface area (ECSA).<sup>1–3,8</sup> One of the major hurdles that needs to be overcome for their practical applications is the sluggish kinetics of the oxygen reduction reaction (ORR) at the cathode.<sup>2–6,8–11</sup> Moreover, considerable activity loss may occur because of carbon corrosion and migration, coalescence, and Ostwald ripening of Pt nanoparticles during fuel-cell operation.<sup>5,12,13</sup>

Recently, a resurgence of interest in unsupported Pt catalysts has occurred. Pt black, consisting of 5–50 nm metallic particles, was the first commercial electrocatalyst for low-temperature fuel cells,<sup>1–3,14</sup> but particle packing results in significantly reduced ECSA. To overcome the drawbacks of particulate forms of both unsupported and supported Pt catalysts, researchers have devoted much effort to the fabrication of self-supported porous Pt nanostructures, including nano-

wires,<sup>15–17</sup> nanotubes,<sup>18,19</sup> nanoflowers,<sup>20,21</sup> nanodendrites,<sup>7,22</sup> hollow spheres,<sup>23–25</sup> and mesoporous particles/films.<sup>26–37</sup> Among them, mesoporous Pt materials are of great interest mainly owing to their interconnected nanostructure and uniform nanometer-scaled porosity that simultaneously facilitates both electron and mass transport (e.g., O<sub>2</sub> and protons)<sup>26–37</sup> and may also increase the residence time of reactant molecules on the metal surface by a confinement effect<sup>38</sup> to enhance the redox reactions. Mesoporous (or nanoporous) metals are promising for fuel cells and other cutting-edge applications such as batteries, supercapacitors, and sensors.<sup>39–43</sup> Recently, significant effort has been made to explore new methods (e.g., dealloying processes<sup>44,45</sup> and hydrothermal synthesis<sup>46</sup>) or to extend the concept of templated synthesis<sup>26–37,39–43</sup> to fabricate meso/nanoporous metals. Compared with other strategies, templated synthesis using ordered mesoporous silica as a hard template remains the most versatile method to prepare ordered mesostructures composed of metals and other compositions, such as oxides and carbon, with controlled structural, textural, and morphological properties.<sup>39–42</sup> A hard template needs to have 3D

Received: July 14, 2013

Revised: September 15, 2013

Published: October 15, 2013



interconnected mesopores to retain an ordered mesostructure in the negatively replicated materials. In addition, a template with smaller pore size is preferred to produce mesoporous metals exhibiting a smaller diameter/size and a higher surface area. Mesoporous MCM-48 silica, a cubic *Ia3d* mesostructure with 3D interpenetrating networks of chiral channels separated by a silica wall,<sup>47–49</sup> is an attractive hard template for mesoporous Pt and other metals.<sup>50–52</sup> However, facile preparation of *Ia3d* mesoporous silica materials remains challenging, and new pathways for the synthesis of MCM-48 nanostructures with controlled size and morphology are desperately needed.<sup>53–55</sup> However, a replication to mesoporous metals with the retention of both mesostructure and morphology, as in the cases of mesoporous carbons,<sup>56–59</sup> is extremely difficult mainly because of a drastic decrease in volume when a metal precursor is reduced.<sup>32–34,39,40,50–52</sup> To the best of our knowledge, the only way to make complete metal replication is through electrodeposition in mesoporous silica films.<sup>36,37</sup>

We herein report a new synthesis of MCM-48 nanospheres and their facile replication to mesoporous Pt nanospheres as a novel self-supported electrocatalyst for the ORR. Kim and co-workers<sup>54</sup> have previously synthesized MCM-48 nanoparticles by using a mixture of cetyltrimethylammonium bromide (CTAB) and ethanol to direct mesostructure formation and triblock copolymer Pluronic F127 as a particle-dispersion agent. In this work, we first discovered a new and simple synthesis of single-crystal-like MCM-48 nanospheres in the absence of ethanol and any dispersion agent. Furthermore, for the first time, we successfully prepared negative Pt replica of MCM-48 nanospheres by a simple and facile process of molten salt impregnation. The high-surface-area mesoporous Pt nanospheres are thermally stable in air and exhibit excellent electrocatalytic activity for the ORR. The results not only show the potential for the mesoporous Pt nanospheres in fuel-cell applications but also reveal directions in materials design to improve further the electrocatalytic performance of this type of self-supported mesoporous Pt catalysts.

## 2. EXPERIMENTAL SECTION

**Synthesis of Mesoporous MCM-48 Silica Nanospheres (M48N).** Benzylcetyldimethylammonium chloride (BCDAC, 1.32 g) was dissolved in a mixture of H<sub>2</sub>O (580 mL) and a sodium hydroxide solution (22 mL, 0.4 mol L<sup>-1</sup>) at 35 °C. Tetraethyl orthosilicate (TEOS, 6.0 mL) was then injected into the solution using a syringe pump at a controlled rate of 7.5 mL h<sup>-1</sup>. The mixture was stirred at 35 °C for 2 h and was then aged at 90 °C for 24 h. The resulting solid was filtered and washed with distilled water (100 mL) followed by ethanol (reagent grade, 50 mL). The surfactants in the as-synthesized sample (1.0 g) were removed by extraction in a mixture of concentrated hydrochloric acid (1.0 mL) and ethanol (100 mL). The product was filtered, washed with ethanol (100 mL), and dried at 60 °C.

**Preparation of Mesoporous Pt Nanospheres (MNPt).** M48N (0.10 g) was mixed with chloroplatinic acid hexahydrate (H<sub>2</sub>PtCl<sub>6</sub>·6H<sub>2</sub>O, 0.58 g) in a glass vial. The mixture was kept at 90 °C for hours to allow the molten salt to infiltrate into the nanospheres. Subsequently, the mixture was heated at 200 °C for 3 h in a stream of hydrogen to reduce the metal. The silica template in the composite Pt@M48N was dissolved by a hydrogen fluoride solution, and the pure-Pt product, MNPt, was repeatedly washed with water and ethanol before being dried and stored in air.

**Materials Characterization.** SEM images were obtained with a field-emission JEOL JSM-7000F microscope operated at 10 kV (for M48N) or 15 kV (for Pt@M48N) or a field-emission JEOL JSM-7600F microscope operated at 15 kV (for MNPt). The pure-silica

M48N was sputter-coated with thin Pt before SEM measurements; the Pt-containing samples Pt@M48N and MNPt were analyzed directly without any coating. TEM images were recorded using a JEOL JEM-2010 microscope operated at 200 kV. XRD patterns were obtained with a Cu K $\alpha$  X-ray source using a Mac Science 18MPX diffractometer. N<sub>2</sub> physisorption isotherms were measured at 77 K using a Quantachrome Autosorb-1-MP instrument. The desorption branches were analyzed by the Barrett–Joyner–Halenda (BJH) method to evaluate pore sizes, and the adsorption branches in the relative pressure range of 0.05–0.30 were used to calculate surface areas by the Brunauer–Emmett–Teller (BET) method. Pore volumes were evaluated at a relative pressure of 0.90. Thermogravimetric analysis (TGA) was performed on a Linseis STA PT1600 analyzer.

**In Situ XAS Studies on Mesoporous Pt Nanospheres.** XAS measurements at the Pt L<sub>3</sub>-edge (11564 eV) were carried out in the transmission mode on the beamline 01C1 of the National Synchrotron Radiation Research Center (NSRRC, Taiwan) with a storage ring energy of 1.5 GeV. For the measurements, MNPt was mixed with boron nitride to result in a sample with ~14 wt % of Pt, and the sample (10 mg) was pressed to form a wafer to be mounted in an *in situ* cell. The sample was heated in air or N<sub>2</sub> at 150 or 300 °C for 30 min and was then cooled to 25 °C for the measurements. XAS spectra were taken in the step scanning mode, and multiple scans were obtained to improve the signal-to-noise ratio.

**Electrochemical Measurements.** The electrochemical measurements were conducted in a thermostatted three-compartment electrochemical cell using a glassy carbon RDE with rotation control (Pine Instrument) connected to a CHI611C potentiostat (CH Instruments). A saturated calomel electrode and a Pt wire were used as reference and counter electrodes, respectively. All potentials were converted to values with reference to the RHE.

The electrochemical properties of MNPt and reference samples including carbon-supported Pt/C (E-TEK, 20 wt %) and Pt black (Aldrich, fuel-cell grade) were measured. For MNPt, the working electrode was prepared by transferring an aqueous dispersion of the sample (1.64 mg mL<sup>-1</sup>) onto the RDE (with a geometric electrode area of 0.196 cm<sup>2</sup>). The Pt loading was 32.7 g (or 166.8 g cm<sup>-2</sup>). The aqueous dispersion was sonicated for 5 min prior to use. Upon drying in air for 2 h, the electrode was covered with a Nafion solution (15 L, 0.05 wt %, prepared by diluting 5 wt % solution from Aldrich) to attach the catalyst particles to the RDE. For Pt black, the working electrode with a Pt loading of 8.0 g (or 40.8 g cm<sup>-2</sup>) was prepared with an aqueous dispersion (0.40 mg mL<sup>-1</sup>) following the same procedure. For Pt/C, an ethanol dispersion (1.00 mg mL<sup>-1</sup>) was sonicated and used to prepare the working electrode with a Pt loading of 3.0 g (or 15.3 g cm<sup>-2</sup>).

The newly prepared electrode was transferred to the electrochemical cell and immersed in an aqueous solution of HClO<sub>4</sub> (0.1 M, diluted from 70% solution from Baker (ACS reagent grade) using Millipore ultrapure water) under a N<sub>2</sub> flow (Linde, ultrahigh purity) at 25 °C for cyclic voltammetry measurements. The potential was continuously cycled between 0 and 1.2 V versus RHE at a rate of 50 mV s<sup>-1</sup> until a stable cyclovoltammogram was recorded. The specific ECSA was estimated by a hydrogen adsorption/desorption method using the following equation

$$\text{specific ECSA} = \frac{Q_H}{mq_H}$$

where  $Q_H$  is the charge associated to H<sub>upd</sub> (between 0 and 0.37 V versus RHE) after double-layer correction,  $m$  is the Pt loading amount, and  $q_H$  is the charge required for monolayer hydrogen adsorption on Pt (210 C cm<sup>-2</sup>). The ORR measurements were performed in the O<sub>2</sub>-saturated HClO<sub>4</sub> solution at 25 °C under a flow of O<sub>2</sub> (Linde, ultrahigh purity) with a RDE rotation rate of 1600 rpm and a potential sweep rate of 10 mV s<sup>-1</sup>. In the polarization curve for the ORR, current densities were normalized in reference to the geometric electrode area. The kinetic current ( $i_k$ ) was derived by applying the Koutecky–Levich equation

$$\frac{1}{i} = \frac{1}{i_k} + \frac{1}{i_d}$$

where  $i$  is the experimentally measured current and  $i_d$  is the diffusion-limiting current. The kinetic current was normalized to the Pt loading amount and specific ECSA to obtain mass activity and specific activity, respectively. The accelerated durability tests were carried out at 25 °C in the O<sub>2</sub>-saturated aqueous solution of H<sub>2</sub>SO<sub>4</sub> (0.5 M, diluted from 97% solution from Showa (reagent grade) using Millipore ultrapure water) by applying cyclic potential sweeps between 0.6 and 1.1 V versus RHE at a rate of 50 mV s<sup>-1</sup> for 2000 and 4000 cycles.

### 3. RESULTS AND DISCUSSION

**3.1. Synthesis of Mesoporous MCM-48 Silica Nanospheres.** The synthesis was performed in a dilute and alkaline solution of benzylcetyldimethylammonium chloride (BCDAC). BCDAC has a nearly identical tail length ( $l$ ) and volume ( $V$ ) as compared to CTAB, but the additional  $\pi$ - $\pi$  interactions between the benzyl groups of the adjacent molecules would slightly compensate for the repulsion between the quaternary ammonium head groups, rendering the surfactant with a smaller effective headgroup area ( $a_0$ ) and slightly larger packing parameter  $g$  (defined as  $g = V/a_0l$ ).<sup>49,60</sup> We expected that upon interacting with anionic silicate species BCDAC alone at very low concentrations (<0.3 wt %) might be able to direct the formation of ordered mesostructures with a mean interfacial curvature lower than that of a 2D hexagonal mesophase while at the same time having a uniform size and morphology. We noted that BCDAC has been used to synthesize MCM-48 by Huo and co-workers,<sup>49</sup> but the synthesis conditions were not the same (with >1.1 wt % BCDAC), and the morphology of the material was not reported and controlled. Indeed, the synthesis resulted in a sample (designated as **M48N**) with a yield of ~75% (on the basis of silica weight, determined by TGA) and excellent structural order.

**M48N** shows more than eight peaks in its X-ray diffraction (XRD) pattern that can be perfectly indexed as the reflections of a cubic  $Ia3d$  structure with a unit cell constant of 9.4 nm (Figure 1). The sample also exhibits a type IV nitrogen physisorption isotherm with a sharp step at a relative pressure ( $p/p_0$ ) of around 0.36, corresponding to the capillary

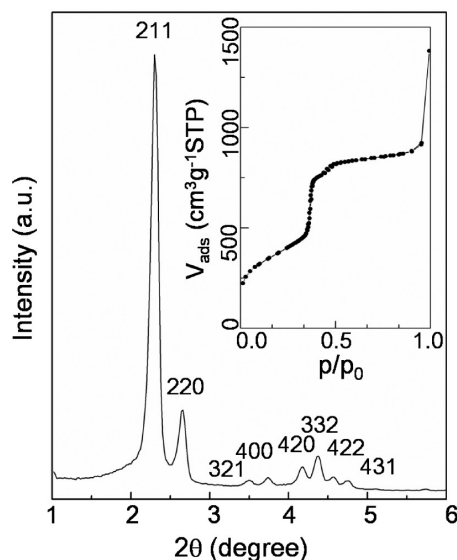


Figure 1. XRD pattern and N<sub>2</sub> physisorption isotherm of **M48N**.

condensation in channel-type mesopores with a diameter of 3.0 nm. On the basis of the unit-cell constant and the pore diameter,<sup>54</sup> the thickness of the silica wall is estimated to be 1.5 nm. The physisorption data further provide a surface area of 1241 m<sup>2</sup> g<sup>-1</sup> and a mesopore volume of 1.25 cm<sup>3</sup> g<sup>-1</sup> for **M48N**. Another step at  $p/p_0 > 0.95$  corresponds to the N<sub>2</sub> condensation in the interparticle voids.

Scanning electron microscopy (SEM) analysis revealed that **M48N** mainly comprises spherical particles with diameters of 200–300 nm (Figure 2a). The interparticle voids may account

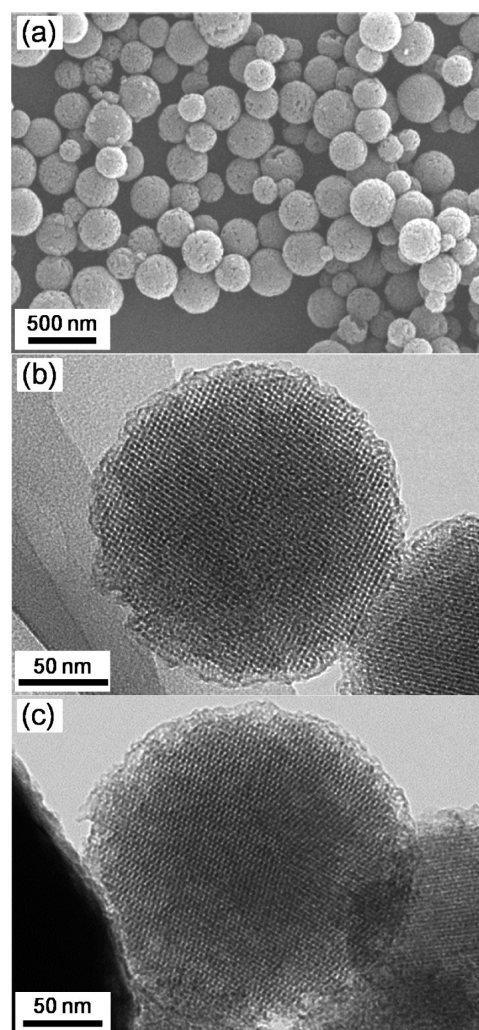


Figure 2. SEM (a) and TEM (b, c) images of **M48N**.

for the appearance of the capillary condensation step at  $p/p_0 > 0.90$  in the N<sub>2</sub> physisorption isotherm. Furthermore, transmission electron microscopy (TEM) analysis suggests that each nanosphere is single-crystal-like with ordered mesostructure extending over the whole particle.

Figures 2b and 2c show typical TEM images of the nanospheres in which the projections along the [100] (Figure 2b) and [311] (Figure 2c) directions of the  $Ia3d$  structure can be clearly observed throughout the nanospheres. The nanospheres do not exhibit truncated facets, a feature for highly crystalline MCM-48 materials,<sup>53,55</sup> but instead have a very rough surface with discernible cavities that may be associated with the tiny capillary condensation step at  $p/p_0 \sim 0.50$  (cf. Figure 1). Exactly how the observed surface cavities were



formed is unknown, but it might arise from possible structural transformation during the cooperative assembly of the diluted cationic surfactant and anionic silicate species under alkaline conditions.<sup>61–63</sup> Nevertheless, the results clearly show that BCDAC can be a good structure-directing agent for the facile synthesis of highly ordered MCM-48 nanospheres.

**3.2. Replication to Mesoporous Platinum Nanospheres.** We then carried out molten salt impregnation to prepare mesoporous Pt nanospheres using the MCM-48 nanospheres as the hard template. Molten salt impregnation does not need any solvent and may allow the impregnated salt to interact directly with the surface of the hard template, but the method has rarely been implemented to fabricate mesoporous Pt and other metals. We chose  $\text{H}_2\text{PtCl}_6 \cdot 6\text{H}_2\text{O}$  for the impregnation because of its low melting point of around 60 °C. Interestingly, we found that the salt in an amount of up to a value corresponding to a complete filling of mesopores of M48N could be incorporated into the hard template, resulting in a dry and orange-colored powder by heating the mixture of the salt and M48N at 90 °C, and that nearly all of the metal remained in the mesopores after hydrogen reduction. As an attempt to make Pt replica nanostructures, we further increased the amount of  $\text{H}_2\text{PtCl}_6 \cdot 6\text{H}_2\text{O}$  in the impregnation process and, to our surprise, nearly all of the reduced metal still stayed inside the hard template. A composite with ~70 wt % Pt loading (designated as Pt@M48N) was prepared accordingly, and its small-angle and wide-angle XRD patterns are shown in Figure 3. The small-angle XRD pattern resembles that of M48N, but

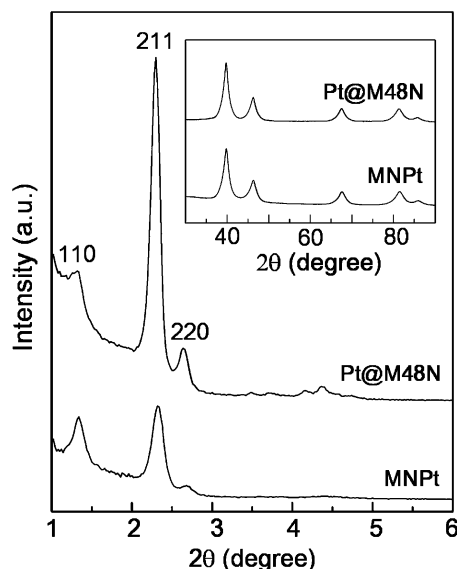


**Figure 3.** Small-angle and wide-angle (inset) XRD patterns of Pt@M48N (~70 wt % Pt) and MNPt.

the intensity of all of the peaks decreases. Additionally, a weak peak appears at  $2\theta = 1.32^\circ$ , corresponding to the (110) reflection of the  $Ia3d$  mesophase that should be symmetrically forbidden. The phenomenon could be attributed to the incomplete filling of the reduced metal in the two chiral channel systems of the bicontinuous mesostructure.<sup>50–52</sup> However, Pt@M48N exhibits very broad peaks in the wide-angle regime, indicating the nanocrystalline nature of Pt in the composite. The average crystalline domain size of Pt is estimated to be 6.5 nm from the width of Pt(111) reflection by the Scherrer equation, assuming spherical crystallite

shapes.<sup>51,52,55</sup> The fact that the estimated value is larger than the mesopore diameter of M48N may be due to the strain and shape effects from X-ray analysis.<sup>51,52</sup> Without additional conductive coating, Pt@M48N was further subjected to SEM analysis so that the metal in the composite appears with bright contrast in the images. Surprisingly, as shown in Figure 4a, we

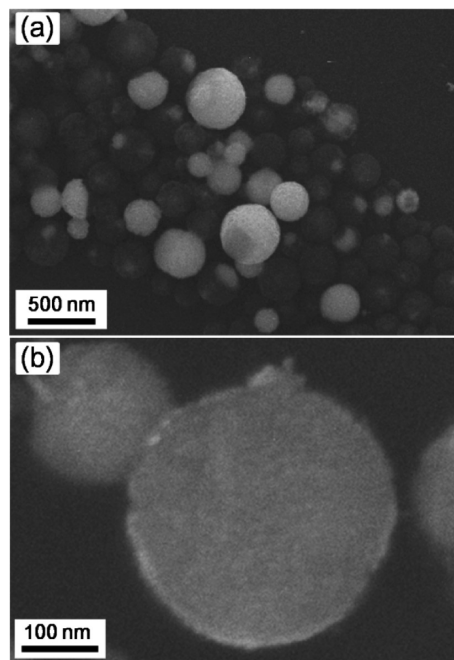


**Figure 4.** (a) SEM image of Pt@M48N. (b) SEM image of the ultramicrotomed nanospheres.

observed that the metal is not evenly distributed in every templating nanosphere, but instead it tends to concentrate in some of them and fills almost completely the mesopores in those nanospheres, as evidenced by the SEM images of the ultramicrotomed sample (Figure 4b). The high degree of pore filling of Pt has never been achieved by other sophisticated methods involving, for example, preformation of Pt nuclei in the mesopores<sup>50</sup> or functionalization of mesopore surface with functional groups that strongly interact with Pt and metal precursor.<sup>51</sup>

The silica template was dissolved by hydrogen fluoride, resulting in the pure-Pt sample MNPt. Both the ordered mesostructure and nanocrystalline nature of Pt were retained in MNPt, as indicated by XRD (cf. Figure 3). In comparison to the XRD pattern of Pt@M48N, it is noted that the (110) reflection of the  $Ia3d$  structure becomes more intense, whereas other reflections are significantly weakened. This can be attributed to a transformation of the mesostructure to a new correlated one (such as cubic  $I4_132$ ) that allows the reflection, which is caused by the displacement of the two sets of Pt nanowires after silica removal.<sup>50–52,56,59</sup> MNPt mainly consists of spherical particles with sizes that are very close or slightly smaller than the diameters of the nanospheres in M48N (Figure 5a). Some truncated nanospheres and large fragments of mesoporous Pt are also found. From high-magnification SEM images, periodically arranged Pt nanowires replicated from the ordered mesostructure of MCM-48 can be directly observed on the mesoporous Pt nanospheres (Figure 5b) or in the truncated nanospheres (Figure 5c) and mesoporous Pt fragments (Figure 5d). The observed nanowire width of 3 nm

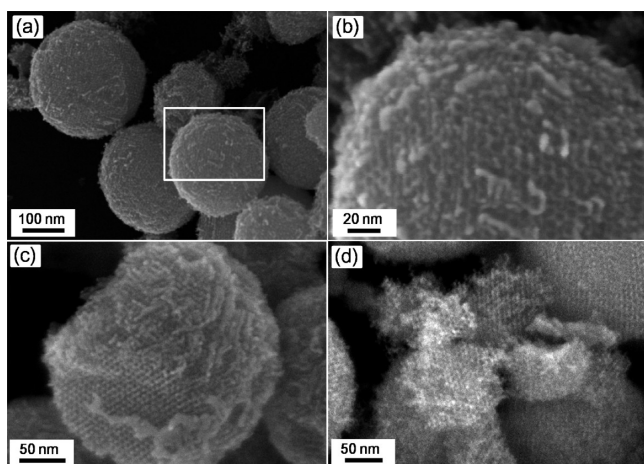


Figure 5. SEM images of MNPt.

is in good agreement with the mesopore diameter of **M48N**. As shown in Figure 6, **MNPt** exhibits a type IV-like  $N_2$

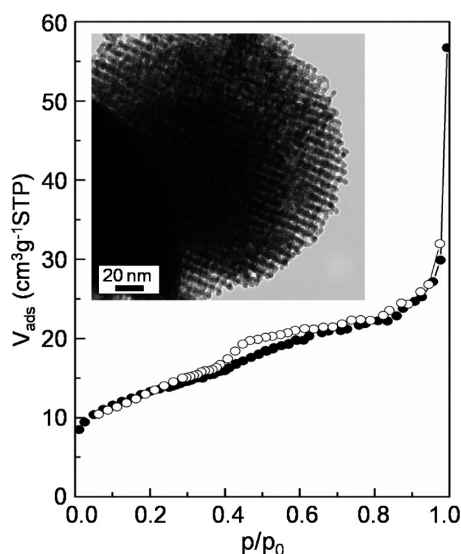


Figure 6.  $N_2$  physisorption isotherm and TEM image of **MNPt**.

physisorption isotherm with H2-type hysteresis loop at  $p/p_0 = 0.40\text{--}0.64$  and sharp step at  $p/p_0$  above 0.90. The sharp step

corresponds to  $N_2$  condensation in the interparticle voids, which also reflects the small size of mesoporous Pt nanospheres. The pore diameter derived from the BJH analysis on the desorption branch is 3.2 nm, and it is larger than the silica wall thickness (1.5 nm) and the gap ( $\sim 1.6$  nm) between 3 nm wide Pt nanowires, as directly observed by TEM (cf. inset in Figure 6). The difference and the appearance of H2-type hysteresis loop may be associated with the displacement of Pt nanowires and a possible incomplete pore filling of Pt in the double gyroid channels, leaving cage-type cavities after silica removal. The surface area of **MNPt** estimated by the BET method is  $50.3\text{ m}^2\text{ g}^{-1}$ , which is somewhat lower than the value ( $\sim 62\text{ m}^2\text{ g}^{-1}$ ) calculated for straight 3 nm wide Pt nanowires but is reasonably high for the sample consisting of 3D interconnected Pt nanowire networks.

The successful replication of MCM-48 nanospheres to mesoporous Pt nanospheres seems to be associated with the speciation of the chloroplatinic complexes during and after molten salt impregnation as well as with the reduction profile. By applying  $^{195}\text{Pt}$  NMR, X-ray absorption spectroscopy (XAS), and other techniques, Lambert and co-workers studied the adsorption of  $\text{H}_2\text{PtCl}_6$  on amorphous silica and the evolution of  $\text{Pt}^{4+}$  speciation upon drying and rewetting.<sup>64</sup> They found that the  $[\text{PtCl}_6]^{2-}$  anions first formed inner-sphere complexes (ISCs) ( $[\text{PtCl}_5(\text{SiOH})]^-$  and  $[\text{PtCl}_4(\text{SiOH})_2]$ ) with the silanol groups on the silica surface at  $90^\circ\text{C}$  and subsequently reacted with water to form outer-sphere complexes (OSCs) ( $[\text{PtCl}_5(\text{H}_2\text{O})]^-$  and  $[\text{cis-PtCl}_4(\text{H}_2\text{O})_2]$ ) upon exposure to ambient humidity at room temperature. They also found that the  $[\text{cis-PtCl}_4(\text{H}_2\text{O})_2]$  OSC could be reduced in a dilute hydrogen flow (5% in argon) at  $10^\circ\text{C}$ .<sup>64</sup> The characterization results of **Pt@M48N** (and also **MNPt**) suggest that similar phenomena may take place during the reduction of the molten-salt-impregnated sample. As schematically shown in Figure 7, a large amount of molten  $\text{H}_2\text{PtCl}_6 \cdot 6\text{H}_2\text{O}$  would fill all of the mesopores in MCM-48 nanospheres and interparticle voids in the nanosphere aggregates at  $90^\circ\text{C}$ . The salt at this temperature may interact with surface silanols to form the aforementioned ISCs that further transform to corresponding OSCs, including  $[\text{cis-PtCl}_4(\text{H}_2\text{O})_2]$ , when the sample is cooled under ambient conditions. Upon exposure to hydrogen at  $25^\circ\text{C}$ , the  $[\text{cis-PtCl}_4(\text{H}_2\text{O})_2]$  species, which is close to the mesopore openings that are directly exposed to the gas phase instead of immersed in  $\text{H}_2\text{PtCl}_6 \cdot 6\text{H}_2\text{O}$  (cf. Figure 7), may get reduced to form Pt nanoparticles. Indeed, we observed a partial

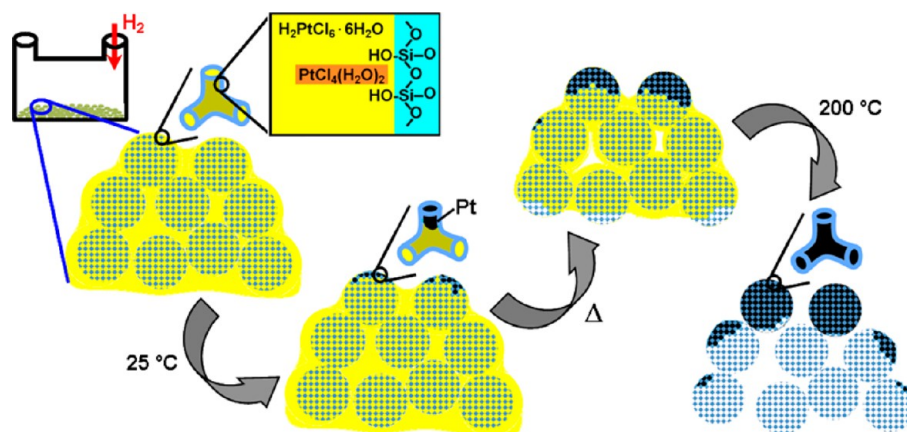


Figure 7. Schematic representation of the reduction process to form **Pt@M48N**.

color change of the sample from orange to gray at this stage of the reduction process. As the temperature starts to increase to 200 °C, the metal salt in proximity to the Pt nanoparticles may be preferentially reduced to result in a continuous growth of the metal in the channels,<sup>50</sup> and the space originally occupied by the salt being reduced may then be refilled by the molten  $\text{H}_2\text{PtCl}_6 \cdot 6\text{H}_2\text{O}$ . As a result, most of the nanospheres in the outmost part of nanosphere aggregates are finally filled almost completely with Pt, whereas those inside the aggregates contain nearly no metal or only small amounts of Pt in the channels. The templated synthesis of Pt replica involving simple molten salt impregnation and facile hydrogen reduction should be applicable for the fabrication of various mesoporous Pt nanostructures with other silica materials with 3D interconnected mesopores.

**3.3. Thermal Stability Studies of MNPt.** Mesoporous Pt nanospheres are promising for PEMFCs, PAFCs, and a variety of cutting-edge applications.<sup>1–5,42,43</sup> For PAFCs and some applications, the self-supported metal nanostructures have to be stable against sintering at elevated temperatures to retain their textural and morphological properties. With such a concern, we employed XAS to characterize MNPt and the samples after being heated at 150 and 300 °C in air. Figure 8a shows the normalized X-ray absorption near-edge structure (XANES) spectra at Pt  $L_3$ -edge (11564 eV) of the samples as well as Pt foil and  $\text{PtO}_2$  powder as references. The spectra suggested that most of the Pt in the MNPt samples is in the reduced form.<sup>65</sup> The white-line intensity slightly increased when MNPt was heated at 150 and 300 °C, and the phenomenon may be

correlated with further oxidation of surface atoms at elevated temperatures.<sup>65</sup>

The extended X-ray absorption fine structure (EXAFS) part of the spectra was further analyzed, and the Fourier transform (FT) profiles of the  $k^3$ -weighted EXAFS data and the curve fitting results of the MNPt samples are shown in Figure 8b and Table S1 in the Supporting Information. The FT profile of the sample before heating (at 25 °C) mainly consists of a first-shell peak corresponding to the Pt–O distance ( $R$ ) of 2.01 Å and a second-shell Pt–Pt peak ( $R$  = 2.75 Å), and the coordination numbers (CN) obtained from data fitting are 0.6 and 8.5, respectively. The presence of the Pt–O peak indicates that mesoporous Pt nanospheres are prone to surface oxidation upon exposure to air.<sup>65</sup> The average Pt particle size estimated from  $\text{CN}_{\text{Pt-Pt}}$  on the basis of a face-centered cubic Pt structure and a spherical model<sup>65,66</sup> is 1.7 nm, which is in reasonably good agreement with the values obtained from XRD and TEM. However, the FT profiles of the heated samples changed only slightly, and a drop in  $\text{CN}_{\text{Pt-Pt}}$  to 7.9 accompanied by a minute increase in  $\text{CN}_{\text{Pt-O}}$  to 0.7 was found for the sample heated at 300 °C. The results suggest that MNPt is thermally stable in air up to 300 °C without significant change in the coordinations of the nanostructured metal. The thermal stability seems to be associated with surface oxidation of the nanostructured Pt that prevents metal sintering.<sup>65</sup> We performed a control experiment in which MNPt was heated in  $\text{N}_2$  and found that the metal was fully reduced and already started to sinter at a temperature of 150 °C (cf. Figure S1 and Table S1 in the Supporting Information). At 300 °C, the nanospheres heated in  $\text{N}_2$  were observed to be melted and deformed, whereas those heated in air retained the spherical shape (cf. Figure S2 in the Supporting Information).

### 3.4. Electrocatalytic Studies of the Oxygen Reduction Reaction.

The electrocatalytic properties of MNPt toward the ORR were benchmarked against commercial Pt/C (E-TEK, 20 wt % 3.2 nm Pt nanoparticles on Vulcan XC-72 carbon) and Pt black (Aldrich, fuel-cell grade). The measurements were obtained in a rotating-disk electrode (RDE) configuration with Pt loadings of 166.8, 40.8, and 15.3  $\text{g cm}^{-2}$  for MNPt, Pt black, and Pt/C, respectively. The loading for MNPt with 3D nanostructure was higher than that for Pt black to cover the entire area of the RDE. Figure 9a shows cyclic voltammetry (CV) curves of these catalysts recorded at 25 °C in  $\text{N}_2$ -purged 0.1 M aqueous solutions of perchloric acid ( $\text{HClO}_4$ ) from 0 to 1.2 V versus the reversible hydrogen electrode (RHE) at 0 rpm and 50  $\text{mV s}^{-1}$ . The region between 0 and 0.37 V for the CV curves is associated with the reversible adsorption/desorption of the underpotentially deposited hydrogen ( $\text{H}_{\text{upd}}$ ). All of the samples exhibited multiple peaks attributed to low-index Pt facets. For MNPt, notably, the characteristic peak of the {110} facets at 0.125 V<sup>67–71</sup> is much more intense than those for Pt black and Pt/C, suggesting a larger fraction of the facets on MNPt. Additionally, the peak at 0.325 V is probably correlated to some high-index stepped Pt surfaces.<sup>69–71</sup> The presence of relatively high-energy {110} and high-index facets<sup>51</sup> in MNPt may result from the confined growth of the reduced metal in the nanometer-sized and torturous channels of MCM-48 hard template. However, the region above ca. 0.6 V versus RHE is dominated by the reversible adsorption/desorption of the adsorbed hydroxyl species ( $\text{OH}_{\text{ad}}$ ). Careful inspection of the CV curves reveals that the  $\text{OH}_{\text{ad}}$  adsorption/desorption peaks (and the onset) for MNPt are positively shifted by about 29 and 5 mV relative to those for Pt/C and Pt black, respectively.

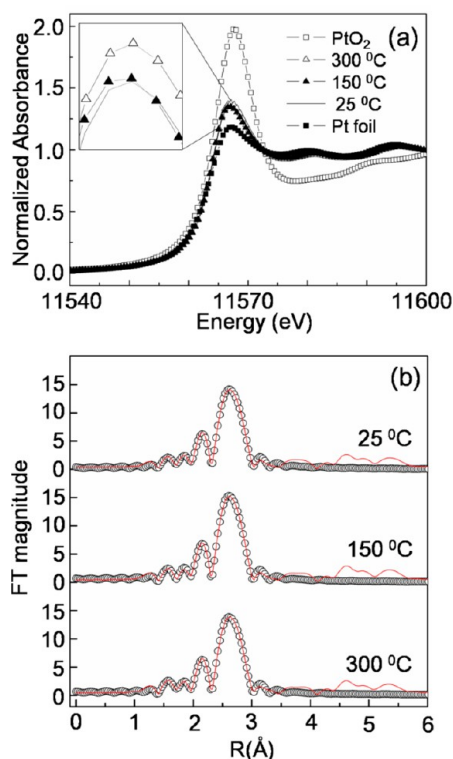


**Figure 8.** (a) Normalized Pt  $L_3$ -edge XANES spectra of the MNPt samples (at 25 °C and being heated at 150 and 300 °C in air), Pt foil, and  $\text{PtO}_2$  powder. (b) Fourier transforms of Pt  $L_3$ -edge  $k^3$ -weighted EXAFS data (red lines) and the fitted results (open circles), respectively, for the MNPt samples. Note that the phase shifts were not corrected.



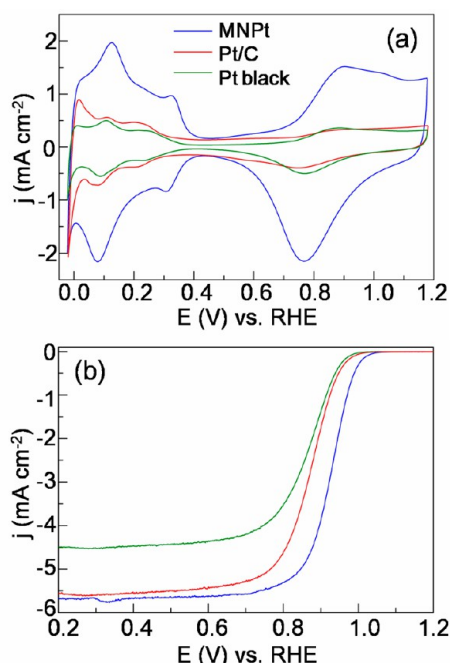


**Figure 9.** (a) CV curves for **MNPt**, Pt/C, and Pt black measured in nitrogen-purged 0.1 M  $\text{HClO}_{4(\text{aq})}$  with a scan rate of  $50 \text{ mV s}^{-1}$ . (b) Polarization curves for the three catalysts measured in oxygen-saturated 0.1 M  $\text{HClO}_{4(\text{aq})}$  with a scan rate of  $10 \text{ mV s}^{-1}$  and a RDE rotating rate of 1600 rpm.

This indicates that the surface sites on **MNPt** do not bind  $\text{OH}_{\text{ad}}$  as strongly as the Pt surface sites on Pt/C and Pt black.

The specific ECSA (the ECSA per unit weight of Pt) was estimated by calculating the charge collected in this  $\text{H}_{\text{upd}}$  adsorption/desorption region with double-layer correction assuming a value of  $210 \text{ C cm}^{-2}$  for the monolayer adsorption of hydrogen on a Pt surface.<sup>6,7</sup> The specific ECSAs of Pt black ( $21.6 \text{ m}^2 \text{ g}_{\text{Pt}}^{-1}$ ) and Pt/C ( $64.9 \text{ m}^2 \text{ g}_{\text{Pt}}^{-1}$ ) were in good agreement with the reported values,<sup>6,7,14,35,37</sup> whereas a value of only  $18.0 \text{ m}^2 \text{ g}_{\text{Pt}}^{-1}$  was measured for **MNPt** with a BET surface area of  $50.3 \text{ m}^2 \text{ g}^{-1}$ . The low specific ECSA may be associated with the effective thickness of the electrical double layer (or the distance between the electrode surface and an equi-potential line in aqueous electrolyte solution), characterized by the Debye length ( $k^{-1}$ ).<sup>72,73</sup> According to the classical Gouy–Chapman theory

$$k = (3.29 \times 10^9) z C^{*1/2}$$

where  $C^*$  is the bulk concentration (in  $\text{mol L}^{-1}$ ) of a symmetrical electrolyte solution of valence  $z$  and  $k$  is given in  $\text{m}^{-1}$ .<sup>72,73</sup> When the radius of the mesopores in **MNPt** is smaller than  $k^{-1}$ , the pore is too narrow for the equi-potential line to follow the geometric surface, and the electrochemically active area would be lower than the geometric area. In our study, the CV measurements were performed in 0.1 M  $\text{HClO}_{4(\text{aq})}$ , and the corresponding value of  $k^{-1}$  is around 1.0 nm, which is slightly larger than half of the gap between Pt nanowires ( $\sim 1.6 \text{ nm}$  as observed by TEM). Because  $k^{-1}$  decreases as the electrolyte concentration increases, we performed a CV measurement in 2.0 M  $\text{HClO}_{4(\text{aq})}$  and indeed found an increase of the specific ECSA to  $24.2 \text{ m}^2 \text{ g}_{\text{Pt}}^{-1}$  (cf. Figure S3 in the Supporting Information for the measured CV curve). The results demonstrate the influence of the effective double-layer

thickness on the specific ECSA of **MNPt** and other mesoporous Pt nanostructures.

The ORR measurements were obtained at  $25^\circ\text{C}$  in  $\text{O}_2$ -saturated 0.1 M  $\text{HClO}_{4(\text{aq})}$  by using a RDE at 1600 rpm and  $10 \text{ mV s}^{-1}$ , and typical ORR polarization curves of the three catalysts are shown in Figure 9b. The diffusion-limiting currents were obtained in the potential region below 0.6 V versus RHE. **MNPt** and Pt/C exhibited similar degrees of deviation from the theoretical limiting current of  $-6.0 \text{ mA cm}^{-2}$ ,<sup>6–9,37</sup> but a positive shift of 43 mV in the half-wave potential (measured at  $j = -2.80 \text{ mA cm}^{-2}$ ) for **MNPt** relative to Pt/C indicates that the catalytic activity of the self-supported **MNPt** was higher than that of carbon-supported nanoparticulate Pt/C. However, a mixed kinetic-diffusion control region exists between 0.7 and 1.0 V versus RHE. The kinetic current derived from the polarization curve by applying the Koutecky–Levich equation<sup>6,7,9,37</sup> was normalized against the ECSA to obtain the specific activity of each catalyst. The specific activity at 0.9 V versus RHE has been applied as a standard metric for evaluating the activities of ORR catalysts.<sup>6,7,9,37</sup> In spite of its low ECSA, **MNPt** exhibited a specific activity of  $0.398 \text{ mA cm}_{\text{Pt}}^{-2}$ , which was 2.7 and 1.8 times greater than that of Pt/C ( $0.147 \text{ mA cm}_{\text{Pt}}^{-2}$ ) and Pt black ( $0.227 \text{ mA cm}_{\text{Pt}}^{-2}$ ). By using the commercial Pt/C as a reference catalyst for comparison, the specific ORR activity of **MNPt** outperformed other mesoporous Pt materials prepared following both soft- and hard-templating routes.<sup>30,37,74,75</sup> The enhanced ORR kinetics for **MNPt** with large fraction of {110} facets could be comprehended by knowing that the ORR activity on low-index facets of Pt in a weakly adsorbing electrolyte (such as  $\text{HClO}_4$ ) increases in the sequence  $\text{Pt}(100) < \text{Pt}(111) < \text{Pt}(110)$ .<sup>7,10,69–71</sup> The fact that **MNPt** exhibited a positively shifted adsorption/desorption peaks of the  $\text{OH}_{\text{ad}}$  species (relative to those for Pt/C and Pt black) also supports the argument that the facet-dependent ORR activity may arise from the structure-sensitive inhibition effect of  $\text{OH}_{\text{ad}}$  species that may block the active site for oxygen adsorption and retard the ORR kinetics.<sup>7</sup> In addition, other factors may also be responsible for the high ORR activity of **MNPt**: the mesopores/interparticle voids in the self-supported catalyst may facilitate mass transport and increase the residence time of reacting species on Pt surface by confinement effect,<sup>38</sup> and the presence of high-index stepped surfaces (as suggested by CV measurements) could favorably adsorb  $\text{O}_2$  molecules to promote the following reduction reactions.<sup>7,69</sup> The kinetic current was also normalized against the amount of Pt to obtain the mass activities of the catalysts. The mass activity of **MNPt** measured at 0.9 V versus RHE ( $0.073 \text{ mA g}_{\text{Pt}}^{-1}$ ) is higher than that of the self-support Pt black ( $0.049 \text{ mA g}_{\text{Pt}}^{-1}$ ), but the value is lower than that of Pt/C ( $0.095 \text{ mA g}_{\text{Pt}}^{-1}$ ) owing to the small ECSA of **MNPt**. Nevertheless, further enhancement in mass activity could be expected for replicated mesoporous Pt materials with larger mesopores.

Finally, we performed accelerated durability tests of **MNPt**, E-TEK Pt/C, and Pt black by applying linear potential sweeps between 0.6 and 1.1 V at  $50 \text{ mV s}^{-1}$  in the  $\text{O}_2$ -saturated  $\text{H}_2\text{SO}_4$  solutions (0.5 M) at  $25^\circ\text{C}$  for 2000 and 4000 cycles. As shown in Figure 10a, **MNPt** exhibited better durability than Pt black and Pt/C. The carbon-supported Pt/C already showed a dramatic decrease (76%) in Pt ECSA in comparison to 43 and 47% loss of ECSA for **MNPt** and Pt black, respectively, after 2000 cycles. After 4000 cycles, **MNPt** lost about 61% of its initial ECSA, whereas a loss of 79% was observed for Pt black.

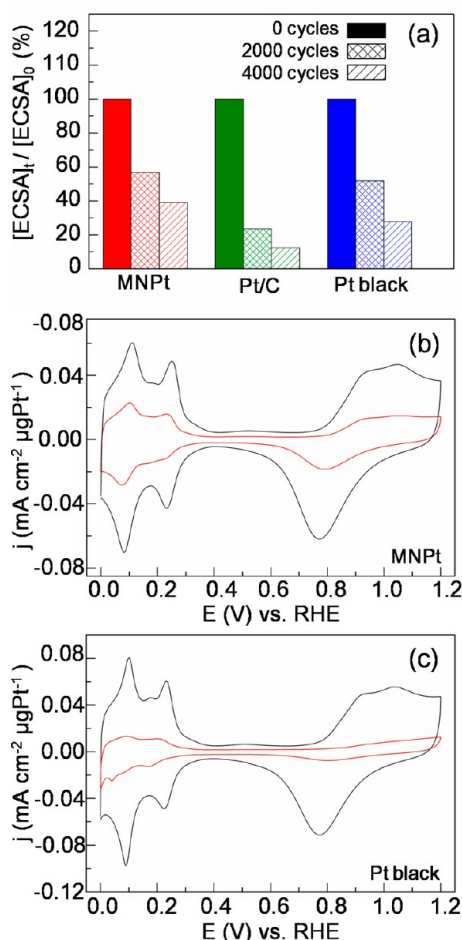


**Figure 10.** (a) Comparison of normalized ECSA of MNPt, Pt/C, and Pt black after 0, 2000, and 4000 cycles in the  $\text{O}_2$ -saturated  $\text{H}_2\text{SO}_{4(\text{aq})}$  (0.5 M). (b, c) CV curves for MNPt (b) and Pt black (c) after 0 (black) and 4000 (red) cycles.

Moreover, as shown in Figure 10b,c, the peaks corresponding to reversible adsorption/desorption of  $\text{H}_{\text{upd}}$  (0–0.3 V versus RHE) and  $\text{OH}_{\text{ad}}$  (0.77 V versus RHE) remained observable for MNPt but became indiscernible for Pt black after 4000 cycles. The results show that the self-supported MNPt has better durability than Pt/C and Pt black and is promising for fuel-cell applications. The results not only show the potential for the mesoporous Pt nanospheres in fuel-cell applications but also reveal directions in materials design to improve further the electrocatalytic performance of this type of self-supported mesoporous Pt catalysts.

#### 4. CONCLUSIONS

We have discovered a new synthesis approach of single-crystal-like MCM-48 nanospheres for the templated preparation of mesoporous Pt nanospheres by molten salt impregnation followed by hydrogen reduction. Mesoporous Pt nanospheres exhibit a high surface area and are thermally stable in air up to 300 °C without showing significant metal sintering. They also have a large fraction of {110} facets and exhibit high electrocatalytic activity for the oxygen reduction reaction. The excellent performance may be mainly attributed to the facet-dependent activities and the presence of interconnected mesopores.

#### ■ ASSOCIATED CONTENT

##### Supporting Information

Pt  $L_3$ -edge EXAFS results for the MNPt samples; normalized Pt  $L_3$ -edge XANES spectra of the MNPt samples, Pt foil, and  $\text{PtO}_2$  powder; Fourier transforms of Pt  $L_3$ -edge  $k^3$ -weighted EXAFS data and the fitted results for the MNPt samples; SEM images of MNPt after heating at 300 °C in air or in  $\text{N}_2$ ; and CV curves for MNPt measured in 0.1 or 2.0 M  $\text{N}_2$ -purged  $\text{HClO}_{4(\text{aq})}$  (PDF). This material is available free of charge via the Internet at <http://pubs.acs.org>.

#### ■ AUTHOR INFORMATION

##### Corresponding Author

\*E-mail: [cmyang@mx.nthu.edu.tw](mailto:cmyang@mx.nthu.edu.tw).

##### Author Contributions

C.M.Y. conceived of the idea of synthesizing MCM-48 nanospheres and preparing platinum replica by molten salt impregnation. N.C.L. synthesized and characterized MCM-48 nanospheres. P.K.C. prepared and characterized platinum replica and conducted XAS studies and electrochemical studies. C.H.H. and Y.W.H. helped P.K.C. perform the XAS and electrochemical studies. J.F.L. assisted in the XAS measurements and data analysis. C.M.Y. supervised the work and wrote the manuscript.

##### Notes

The authors declare no competing financial interest.

#### ■ ACKNOWLEDGMENTS

We thank the Frontier Research Center on Fundamental and Applied Sciences of Matters and the National Science Council of Taiwan (under contract no. NSC101-2628-M-007-001-MY2) for financial support.

#### ■ REFERENCES

- (1) Carrette, L.; Friedrich, K. A.; Stimming, U. *ChemPhysChem* **2000**, *1*, 162–193.
- (2) Steele, B. C. H.; Heinzl, A. *Nature* **2001**, *414*, 345–352.
- (3) Perry, M. L.; Fuller, T. F. *J. Electrochem. Soc.* **2002**, *149*, 59–67.
- (4) Arico, A. S.; Bruce, P.; Scrosati, B.; Tarascon, J. M.; Van Schalkwijk, W. *Nat. Mater.* **2005**, *4*, 366–377.
- (5) Debe, M. K. *Nature* **2012**, *486*, 43–51.
- (6) Gasteiger, H. A.; Kocha, S. S.; Sompalli, B.; Wagner, F. T. *Appl. Catal., B* **2005**, *56*, 9–35.
- (7) Lim, B.; Jiang, M.; Camargo, P. H. C.; Cho, E. C.; Tao, J.; Lu, X.; Zhu, Y.; Xia, Y. *Science* **2009**, *324*, 1302–1305.
- (8) Gasteiger, H. A.; Markovic, N. M. *Science* **2009**, *324*, 48–49.
- (9) Bing, Y.; Liu, H.; Zhang, L.; Ghosh, D.; Zhang, J. *Chem. Soc. Rev.* **2010**, *39*, 2184–2202.
- (10) Markovic, N. M.; Schmidt, T. J.; Stamenkovic, V.; Ross, P. N. *Fuel Cells* **2001**, *1*, 105–116.
- (11) Nørskov, J. K.; Rossmeisl, J.; Logadottir, A.; Lindqvist, L.; Kitchin, J. R.; Bligaard, T.; Jonsson, H. *J. Phys. Chem. B* **2004**, *108*, 17886–17892.
- (12) de Bruijn, F. A.; Dam, V. A. T.; Janssen, G. J. M. *Fuel Cells* **2008**, *8*, 3–22.
- (13) Wang, Y. J.; Wilkinson, D. P.; Zhang, J. *Chem. Rev.* **2011**, *111*, 7625–7651.
- (14) Antolini, E.; Perez, J. *J. Mater. Sci.* **2011**, *46*, 4435–4457.
- (15) Sun, S.; Yang, D.; Villers, D.; Zhang, G.; Sacher, E.; Dodelet, J. P. *Adv. Mater.* **2008**, *20*, 571–574.
- (16) Koenigsmann, C.; Zhou, W. P.; Adzic, R. R.; Sutter, E.; Wong, S. S. *Nano Lett.* **2010**, *10*, 2806–2811.
- (17) Liang, H. W.; Cao, X.; Zhou, F.; Cui, C. H.; Zhang, W. J.; Yu, S. H. *Adv. Mater.* **2011**, *23*, 1467–1471.



- (18) Chen, Z.; Waje, M.; Li, W.; Yan, Y. *Angew. Chem., Int. Ed.* **2007**, *46*, 4060–4063.
- (19) Alia, S. M.; Zhang, G.; Kisailus, D.; Li, D. S.; Gu, S.; Jensen, K.; Yan, Y. S. *Adv. Funct. Mater.* **2010**, *20*, 3742–3746.
- (20) Song, Y. J.; Steen, W. A.; Pena, D.; Jiang, Y. B.; Medforth, C. J.; Huo, Q. S.; Pincus, J. L.; Qiu, Y.; Sasaki, D. Y.; Miller, J. E.; Shelnutt, J. A. *Chem. Mater.* **2006**, *18*, 2335–2346.
- (21) Song, Y.; Hickner, M. A.; Challa, S. R.; Dorin, R. M.; Garcia, R. M.; Wang, H.; Jiang, Y. B.; Li, P.; Qiu, Y.; van Swol, F.; Medforth, C. J.; Miller, J. E.; Nwoga, T.; Kawahara, K.; Li, W.; Shelnutt, J. A. *Nano Lett.* **2009**, *9*, 1534–1539.
- (22) Lin, Z. H.; Lin, M. H.; Chang, H. T. *Chem.—Eur. J.* **2009**, *15*, 4656–4662.
- (23) Liang, H. P.; Zhang, H. M.; Hu, J. S.; Guo, Y. G.; Wan, L. J.; Bai, C. L. *Angew. Chem., Int. Ed.* **2004**, *43*, 1540–1543.
- (24) Chen, H. M.; Liu, R. S.; Lo, M. Y.; Chang, S. C.; Tsai, L. D.; Peng, Y. M.; Lee, J. F. *J. Phys. Chem. C* **2008**, *112*, 7522–7526.
- (25) Ataee-Esfahani, H.; Nemoto, Y.; Wang, L.; Yamauchi, Y. *Chem. Commun.* **2011**, *47*, 3885–3887.
- (26) Attard, G. S.; Bartlett, P. N.; Coleman, N. R. B.; Elliott, J. M.; Owen, J. R.; Wang, J. H. *Science* **1997**, *278*, 838–840.
- (27) Birkin, P. R.; Elliott, J. M.; Watson, Y. E. *Chem. Commun.* **2000**, 1693–1694.
- (28) Park, S.; Lee, S. Y.; Boo, H.; Kim, H. M.; Kim, K. B.; Kim, H. C.; Song, Y. J.; Chung, T. D. *Chem. Mater.* **2007**, *19*, 3373–3375.
- (29) Tominaka, S.; Wu, C. W.; Momma, T.; Kuroda, K.; Osaka, T. *Chem. Commun.* **2008**, 2888–2890.
- (30) Bauer, A.; Wilkinson, D. P.; Gyenge, E. L.; Bizzotto, D.; Ye, S. J. *Electrochem. Soc.* **2009**, *156*, 1169–1174.
- (31) Yamauchi, Y.; Takai, A.; Komatsu, M.; Sawada, M.; Ohsuna, T.; Kuroda, K. *Chem. Mater.* **2008**, *20*, 1004–1011.
- (32) Doi, Y.; Takai, A.; Sakamoto, Y.; Terasaki, O.; Yamauchi, Y.; Kuroda, K. *Chem. Commun.* **2010**, *46*, 6365–6367.
- (33) Han, Y. J.; Kim, J. M.; Stucky, G. D. *Chem. Mater.* **2000**, *12*, 2068–2069.
- (34) Wang, H.; Jeong, H. Y.; Imura, M.; Wang, L.; Radhakrishnan, L.; Fujita, N.; Castle, T.; Terasaki, O.; Yamauchi, Y. *J. Am. Chem. Soc.* **2011**, *133*, 14526–14529.
- (35) van der Vliet, D. F.; Wang, C.; Tripkovic, D.; Strmcnik, D.; Zhang, X. F.; Debe, M. K.; Atanasoski, R. T.; Markovic, N. M.; Stamenkovic, V. R. *Nat. Mater.* **2012**, *11*, 1051–1058.
- (36) Wu, C. W.; Yamauchi, Y.; Ohsuna, T.; Kuroda, K. *J. Mater. Chem.* **2006**, *16*, 3091–3098.
- (37) Kibsgaard, J.; Gorlin, Y.; Chen, Z.; Jaramillo, T. F. *J. Am. Chem. Soc.* **2012**, *134*, 7758–7765.
- (38) Han, J. H.; Lee, E.; Park, S.; Chang, R.; Chung, T. D. *J. Phys. Chem. C* **2010**, *114*, 9546–9553.
- (39) Schuth, F. *Chem. Mater.* **2001**, *13*, 3184–3195.
- (40) Yang, H. F.; Zhao, D. Y. *J. Mater. Chem.* **2005**, *15*, 1217–1231.
- (41) Lu, A. H.; Schueth, F. *Adv. Mater.* **2006**, *18*, 1793–1805.
- (42) Yamauchi, Y.; Kuroda, K. *Chem.—Asian J.* **2008**, *3*, 664–676.
- (43) Walcarius, A. *Anal. Bioanal. Chem.* **2010**, *396*, 261–272.
- (44) Erlebacher, J.; Aziz, M. J.; Karma, A.; Dimitrov, N.; Sieradzki, K. *Nature* **2001**, *410*, 450–453.
- (45) Liu, L.; Pippel, E.; Scholz, R.; Goesele, U. *Nano Lett.* **2009**, *9*, 4352–4358.
- (46) Peng, X. S.; Koczur, K.; Nigro, S.; Chen, A. C. *Chem. Commun.* **2004**, 2872–2873.
- (47) Kresge, C. T.; Leonowicz, M. E.; Roth, W. J.; Vartuli, J. C.; Beck, J. S. *Nature* **1992**, *359*, 710–712.
- (48) Beck, J. S.; Vartuli, J. C.; Roth, W. J.; Leonowicz, M. E.; Kresge, C. T.; Schmitt, K. D.; Chu, C. T. W.; Olson, D. H.; Sheppard, E. W.; McCullen, S. B.; Higgins, J. B.; Schlenker, J. L. *J. Am. Chem. Soc.* **1992**, *114*, 10834–10843.
- (49) Huo, Q.; Margolese, D. I.; Stucky, G. D. *Chem. Mater.* **1996**, *8*, 1147–1160.
- (50) Shin, H. J.; Ryoo, R.; Liu, Z.; Terasaki, O. *J. Am. Chem. Soc.* **2001**, *123*, 1246–1247.
- (51) Yang, C. M.; Sheu, H. S.; Chao, K. J. *Adv. Func. Mater.* **2002**, *12*, 143–148.
- (52) Guo, X. J.; Yang, C. M.; Liu, P. H.; Cheng, M. H.; Chao, K. J. *Cryst. Growth Des.* **2005**, *5*, 33–36.
- (53) Kim, J. M.; Kim, S. K.; Ryoo, R. *Chem. Commun.* **1998**, 259–260.
- (54) Kim, T. W.; Chung, P. W.; Lin, V. S. Y. *Chem. Mater.* **2010**, *22*, 5093–5104.
- (55) Chang, A.; Lai, N. C.; Yang, C. M. *RSC Adv.* **2012**, *2*, 12088–12090.
- (56) Ryoo, R.; Joo, S. H.; Jun, S. J. *J. Phys. Chem. B* **1999**, *103*, 7743–7746.
- (57) Jun, S.; Joo, S. H.; Ryoo, R.; Kruk, M.; Jaroniec, M.; Liu, Z.; Ohsuna, T.; Terasaki, O. *J. Am. Chem. Soc.* **2000**, *122*, 10712–10713.
- (58) Joo, S. H.; Choi, S. J.; Oh, I.; Kwak, J.; Liu, Z.; Terasaki, O.; Ryoo, R. *Nature* **2001**, *412*, 169–172.
- (59) Solovyov, L. A.; Zaikovskii, V. I.; Shmakov, A. N.; Belousov, O. V.; Ryoo, R. *J. Phys. Chem. B* **2002**, *106*, 12198–12202.
- (60) Han, Y.; Zhang, D.; Chng, L. L.; Sun, J.; Zhao, L.; Zou, X.; Ying, J. Y. *Nat. Chem.* **2009**, *1*, 123–127.
- (61) Yang, C. M.; Lin, C. Y.; Sakamoto, Y.; Huang, W. C.; Chang, L. L. *Chem. Commun.* **2008**, 5969–5971.
- (62) Huang, W. C.; Chang, L. L.; Sakamoto, Y.; Lin, C. Y.; Lai, N. C.; Yang, C. M. *RSC Adv.* **2011**, *1*, 229–237.
- (63) Huang, W. C.; Lai, N. C.; Chang, L. L.; Yang, C. M. *Microporous Mesoporous Mater.* **2012**, *151*, 411–417.
- (64) Boujday, S.; Lehman, J.; Lambert, J. F.; Che, M. *Catal. Lett.* **2003**, *88*, 23–30.
- (65) Yang, C. M.; Liu, P. H.; Ho, Y. F.; Chiu, C. Y.; Chao, K. J. *Chem. Mater.* **2003**, *15*, 275–280.
- (66) Jentys, A. *Phys. Chem. Chem. Phys.* **1999**, *1*, 4059–4063.
- (67) Friedrich, K. A.; Daum, W.; Klunker, C.; Knabben, D.; Stimming, U.; Ibach, H. *Surf. Sci.* **1995**, *335*, 315–325.
- (68) Huerta, F. J.; Morallon, E.; Vazquez, J. L.; Aldaz, A. *Surf. Sci.* **1998**, *396*, 400–410.
- (69) Kuzume, A.; Herrero, E.; Feliu, J. M. *J. Electroanal. Chem.* **2007**, *599*, 333–343.
- (70) Solla-Gullon, J.; Rodriguez, P.; Herrero, E.; Aldaz, A.; Feliu, J. M. *Phys. Chem. Chem. Phys.* **2008**, *10*, 1359–1373.
- (71) Subbaraman, R.; Strmcnik, D.; Stamenkovic, V.; Markovic, N. M. *J. Phys. Chem. C* **2010**, *114*, 8414–8422.
- (72) Bard, A. J.; Faulkner, L. R. In *Electrochemical Methods: Fundamentals and Applications*, 2nd ed.; John Wiley & Sons: New York, 2001.
- (73) Boo, H.; Park, S.; Ku, B. Y.; Kim, Y.; Park, J. H.; Kim, H. C.; Chung, T. D. *J. Am. Chem. Soc.* **2004**, *126*, 4524–4525.
- (74) Jiang, J. J.; Kucernak, A. *Electrochem. Solid-State Lett.* **2000**, *3*, 559–562.
- (75) Kucernak, A.; Jiang, J. H. *Chem. Eng. J.* **2003**, *93*, 81–90.